A Journal of the Gesellschaft Deutscher Chemiker

Angewandte International Edition Chemie

GDCh

www.angewandte.org

Accepted Article

Title: Synergy of Cu/C3N4 Interface and Cu Nanoparticles Dual Catalytic Regions in Electrolysis of CO to Acetic Acid

Authors: Xupeng Yan, Menglu Zhang, Yizhen Chen, Yahui Wu, Ruizhi Wu, Qiang Wan, Chunxiao Liu, Tingting Zheng, Rongjuan Feng, Jing Zhang, Chunjun Chen, Chuan Xia, Qinggogn Zhu, Xiaofu Sun, Qingli Qian, and Buxing Han

To be cited as: *Angew. Chem. Int. Ed.* **2023**, e202301507

Link to VoR: https://doi.org/10.1002/anie.202301507

WILEY VCH

10.1002/anie.202301507

WILEY-VCH

Synergy of Cu/C_3N_4 Interface and Cu Nanoparticles Dual Catalytic Regions in Electrolysis of CO to Acetic Acid

Xupeng Yan,[a,b,j]# Menglu Zhang,[c,d]# Yizhen Chen,[h]# Yahui Wu,[a,b] Ruizhi Wu,[a,b] Qiang Wan,[a,b] Chunxiao Liu,[d] Tingting Zheng,[d,e] Rongjuan Feng,[a] Jing Zhang,[i] Chunjun Chen,[a,b]* Chuan Xia,[d,e]* Qinggogn Zhu,[a,b] Xiaofu Sun,[a,b] Qingli Qian,[a,b] and Buxing Han[a,b,f,g]*

[a] Dr. X. Yan, Dr. C. Chen, Dr. Y. Wu, Dr. R. Wu, Dr. Q. Wan, Dr. R. Feng, Prof. Dr. Q. Qian, Prof. Dr. X. Sun, Prof. Dr Q. Zhu and Prof. Dr. B. Han
Beijing National Laboratory for Molecular Sciences, CAS Key Laboratory of Colloid and Interface and Thermodynamics, CAS Research/Education Center for Excellence in Molecular Sciences, Center for Carbon Neutral Chemistry, Institute of Chemistry, Chinese Academy of Sciences
Beijing 100190, China
E-mail: chenchunjun@iccas.ac.cn, chuan.xia@uestc.edu.cn, hanbx@iccas.ac.cn

[b] Dr. X. Yan, Dr. C. Chen, Dr. Y. Wu, Dr. R. Wu, Dr. Q. Wan, Prof. Dr. Q. Qian, Prof. Dr. X. Sun, Prof. Dr Q. Zhu and Prof. Dr. B. Han
School of Chemistry and Chemical Engineering, University of Chinese Academy of Sciences
Beijing 100049, China

[c] M. Zhang
Hefei National Laboratory for Physical Sciences at the Microscale, Department of Chemical Physics, University of Science and Technology of China
Hefei, People's Republic of China

[d] M. Zhang, Dr. C. Liu, Prof. Dr. T. Zheng and Prof. Dr. C. X
School of Materials and Energy, University of Electronic Science and Technology of China
Chengdu, People's Republic of China

[e] Prof. Dr. T. Zheng and Prof. Dr. C. X
Yangtze Delta Region Institute (Huzhou), University of Electronic Science and Technology of China
Huzhou, People's Republic of China

[f] Prof. Dr. B. Han
Physical Science Laboratory, Huairou National Comprehensive Science Center, No. 5 Yanqi East Second Street
Beijing 101400, China

[g] Prof. Dr. B. Han
Shanghai Key Laboratory of Green Chemistry and Chemical Processes, School of Chemistry and Molecular Engineering, East China Normal University
Shanghai 200062, China

[h] Dr. Y. Chen
Department of Chemical Engineering, University of California, Davis
California 95616, United States

[i] Prof. Dr. J. Zheng
Institute of High Energy Physics, Chinese Academy of Sciences
Beijing 100049, China

[j] Dr. X. Yan
China Huaneng Clean Energy Research Institute
Beijing 102209, China

These authors contributed equally: Xupeng Yan, Menglu Zhang, Yizhen Chen

Supporting information for this article is given via a link at the end of the document.

Abstract: Electrochemical reduction reaction of carbon monoxide (CORR) offers a promising way to manufacture acetic acid directly from gaseous CO and water at mild condition. Herein, we discovered that the graphitic carbon nitride (g-C_3N_4) supported Cu nanoparticles (Cu-CN) with the appropriate size showed a high acetate faradaic efficiency of 62.8% with a partial current density of 188 mA cm^{-2} in CORR. *In-situ* experimental and density functional theory calculation studies revealed that the Cu/C_3N_4 interface and metallic Cu surface synergistically promoted CORR into acetic acid. The generation of pivotal intermediate -*CHO is advantage around the Cu/C_3N_4 interface and migrated *CHO facilitate acetic acid generation on metallic Cu surface with promoted *CHO coverage. Moreover, continuous production of acetic acid aqueous solution was achieved in a porous solid electrolyte reactor, indicating the great potential of Cu-CN catalyst in the industrial application.

Introduction

Acetic Acid (CH_3COOH) is a bulk chemical product and one of the most important organic acids, and used as the solvent and reagent to manufacture a variety of chemicals as well as polymeric materials.[1,2] The acetic acid is mainly produced by the methanol carbonylation ($CH_3OH+CO=CH_3COOH$),[3] which requires heating and pressurization as well as expensive Rhodium catalysts. Besides, methanol production generally derives from syngas (CO/H_2) operated at high temperature and pressure.[4] Since carbon monoxide (CO) is necessary in both methanol and acetic acid synthesis, the direct synthesis of acetic acid from gaseous CO would be efficient and economical if possible. Fortunately, the rapid development of renewable energy technology and continuously reduced electricity price drive the possibility to produce valuable chemicals and fuels from CO and water via the electrochemical method.[5,6] Therefore, environmentally benign electrochemical reduction reaction of CO (CORR) is regarded as a promising way to produce acetic acid directly.

Multicarbon (C_{2+}) products can be produced over Cu-based catalysts via CORR,[7,8] but specific catalytic activity towards

acetate production is still low.[7,9] Recently, the Faradaic efficiency (FE) and current density (*j*) of acetate in CORR were significantly promoted by CuPd alloy (the atomic ratio of Cu and Pd is 1:1),[10] whereas the introduction of precious metals increased the cost of catalysts. Besides, in the traditional H-cell or flow-cell reactors, the produced acetate generally mixed with liquid electrolytes (KOH or $KHCO_3$), and further separation and concentration are necessary to gain the purified product.[7,9,11] In recent years, porous solid electrolyte (PSE) reactor seems to be expected to solve above problem and directly acquire the high purity liquid products.[12,13] However, acetic acid FEs in these reactors are still below 45%. Thus, designing low-cost and efficient catalysts towards acetic acid in a PSE reactor is in demand for the practical application.

Given intermediates are key for the specific product selectivity and generally related with the surface properties of catalysts,[14,15] it is rational to design catalysts with proper local environments to facilitate the generation of key intermediates and the target product. Supported catalysts are attractive in heterogenous catalysis for the interfacial effect is generally effective to desired reactions.[16,17] As size increases, the intrinsic property of active component would become non-negligible and offers discrepant local environment from the interface,[18] which makes it possible to gain dual catalytic regions on one supported catalyst to catalyze multistep reactions like CORR.

In this work, we developed a unary supported catalyst, *i.e.,* graphitic carbon nitride (g-C_3N_4) supported copper nanoparticles (Cu-CN), and discovered the correlation between its catalytic performance and the ratio of the interface to active component surface in CORR, which can be adjusted by the size of Cu nanoparticles (Cu NPs). The unary supported catalyst with proper Cu size exhibits a high acetate FE of 62.8% with the partial current density of 188 mA cm^{-2}. Combined with *in-situ* characterizations and density functional theory (DFT) calculation results, we concluded that the formation of acetate undergoes two key steps, *i.e.*, the activation of CO and following coupling step, which occurs on the Cu/C_3N_4 interface and Cu surface (away from interface), respectively. The cooperation of two catalytic regions dramatically accelerates the acetate formation. Direct electrosynthesis of high purity acetic acid (>90%) was achieved over Cu-CN catalysts in a PSE reactor, and CO could be continuously converted into acetic acid with 55.6% FE at a constant current density of 100 mA cm^{-2} for at least 120 h.

Results and Discussion

The Cu-CN catalysts were prepared by blending Cu nanoparticles (Cu NPs) and g-C_3N_4 with the assistance of sonication (see Methods for experimental details), named as Cu(Xnm)-CN-Y (where X presents the size of Cu NPs and Y presents the mass ratio of C_3N_4 to Cu NPs). The Cu NPs with abundant Cu (111) and g-C_3N_4 were prepared respectively according to reported methods,[19,20] and the average size of the as-prepared Cu NPs was about 25 nm while the g-C_3N_4 exhibited the nanosheet morphology (Supplementary Fig. S1 and S2). Firstly, we evaluated CORR catalytic property of the Cu NPs (25nm), g-C_3N_4 and Cu(25nm)-CN-Y catalysts in the flow cell,[21] and 1M KOH was used as electrolyte. Gas and liquid products were detected by gas chromatography (GC) and ^{1}H nuclear magnetic resonance (NMR) (Supplementary Fig. S3 and S4), respectively.

It was noted that the pristine Cu NPs (25nm) exhibited remarkable C_{2+} products (ethylene, ethanol, acetate and *n*-propanol) FEs (>80%) during CORR, but failed to gain high single product selectivity (Supplementary Fig. S5). The maximum acetate FE was only 28.8 % with the partial current density ($j_{acetate}$) of 138 mA cm^{-2} at -0.97 V (versus RHE for all potentials unless specifically noted) (Figure 1a and 1b). On the contrary, acetate FE and corresponding $j_{acetate}$ were significantly promoted over Cu(25nm)-CN-3 from -0.67 V and the maximum acetate FE reached 62.8% with $j_{acetate}$ of 188 mA cm^{-2} at -0.87 V. In the meantime, the proportion of acetate in C_{2+} products over Cu(25nm)-CN-3 was at least twice as that over Cu NPs (25nm) under the applied potential range of -0.67 V to -1.17 V (Supplementary Fig. S6), indicating the enhancement of acetate selectivity and the suppression of other C_{2+} products in the existence of g-C_3N_4. The FEs of various products over the Cu NPs (25nm) and Cu(25nm)-CN-3 were listed in Supplementary Table S1. Above results confirm that the combination of Cu NPs and g-C_3N_4 is effective towards the multistep CO-to-acetate reaction. Relative to the state-of-the-art catalysts, Cu(25nm)-CN-3 performs as one of the best catalysts towards acetate in CORR (Figure 1c and Supplementary Table S2).

The role of the g-C_3N_4 on the acetate selectivity was investigated by varying the mass ratio of g-C_3N_4 and Cu NPs in the Cu-CN catalysts. Bulk g-C_3N_4 had the poor capacity to catalyze CO into acetate ($FE_{acetate}$ < 10%) (Figure 1d). We can observe that the acetate FEs varied with the mass ratio of g-C_3N_4 to Cu NPs (Figure 1d). Moreover, the potential for the peak $FE_{acetate}$ over the Cu-CN catalysts also positively shifted compared to that on Cu NPs, indicating the positive effect of g-C_3N_4 towards acetate selectivity. Among Cu-CN catalysts, Cu(25nm)-CN-3 showed best selectivity and activity towards acetate (Figure 1d and Supplementary Fig. S7 and S8). Thus, we can conclude that the catalytic activity for acetate over the supported catalyst was correlated with both Cu NPs and g-C_3N_4.

To reveal the intrinsic activity towards acetate of the catalysts, the electrochemical active surface areas of Cu (Cu_{ECSAs}) were determined by the lead (Pb) under potential deposition (UPD) and used to normalize the current density (Supplementary Fig. S9 and Table S3).[22,23] As expected, Cu-CN catalysts displayed higher acetate ECSA corrected current density (j_{ecsa}) than Cu NPs (Figure 1e) at all applied potentials, confirming the promotion of the intrinsic activity towards acetate in the presence of g-C_3N_4. It is worth noting that the acetate j_{ecsa} over Cu(25nm)-CN-6 and Cu(25nm)-CN-3 were similar at the low potentials, while it dropped considerably over Cu(25nm)-CN-1 with a high Cu NPs loading amount, which was probably ascribed to the restricted formation of interfaces induced by the aggregation of Cu NPs on Cu(25nm)-CN-1 (Supplementary Fig. S10). Hence, we speculated that the Cu was the main active sites for the acetate production and the corresponding intrinsic activity could be enhanced by g-C_3N_4, which was likely from the synergistic effect between the Cu NPs and g-C_3N_4.

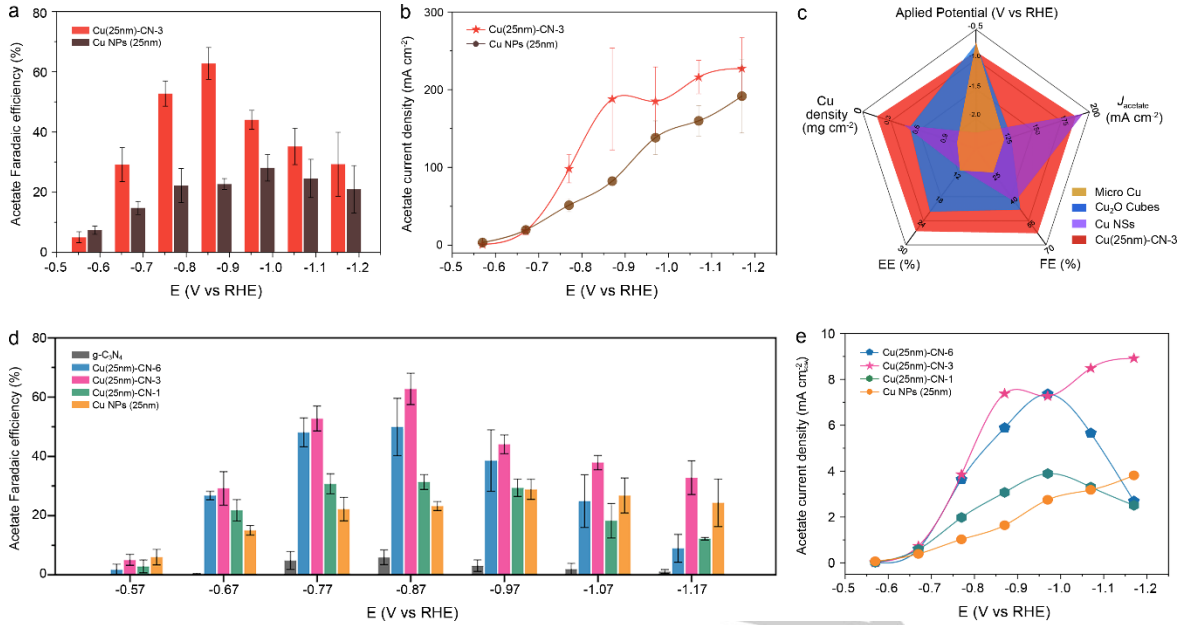

Figure 1. CORR performance over Cu-CN catalysts. a, b, Acetate FE and corresponding partial current density over Cu(25nm)-CN-3 and Cu NPs (25nm) at various applied potentials. c, Comparison of state-of-art catalysts towards acetate in CORR (Supplementary Table. S2). d, e, Acetate FE and corresponding ECSA normalized acetate partial current density over Cu-CN catalysts with various mass ratio of g-C_3N_4 to Cu at various applied potentials.

Since the chemical state of Cu often acts as an important role in catalysis, *in-operando* X-ray adsorption spectroscopy (XAS) measurements were recorded to track the oxidation state and local bonding environments of the Cu during CORR. During CORR, X-ray absorption near edge structure (XANES) spectra of Cu NPs (25nm) and Cu(25nm)-CN-3 exhibit the similar feature as Cu foil, indicating that the metallic Cu was dominated in Cu NPs (25nm) and Cu(25nm)-CN-3 catalysts (Supplementary Fig. S11a). In addition, modeling of the EXAFS data also indicated that only metallic Cu species existed in Cu NPs (25nm) and Cu(25nm)-CN-3 during CORR (Supplementary Fig. S11b, Supplementary Fig. S12, Table S4 and S5). The *in-operando* EXAFS data showed that the Cu species were characterized by a Cu-Cu coordination numbers of 10-11 at a bonding distance of 2.53-2.54 Å at various negative potential (-0.47, -0.67 and -0.87 V) in both Cu NPs (25nm) and Cu(25nm)-CN-3, indicating that the catalytic Cu active sites over Cu NPs (25nm) and Cu(25nm)-CN-3 exhibited similar oxidation state and coordination environments during CORR.

To further screen the mechanism and clarify the performance divergence towards acetate over Cu NPs and Cu-CN in CORR, the density functional theory (DFT) calculations were conducted. According to the characterization of prepared Cu NPs and Cu-CN catalysts, Cu(111) and Cu(111)/C_3N_4 models were constructed to represent the Cu NPs and Cu-CN catalysts (Supplementary Fig. S13). For the of Cu-CN catalysts, we chosen the Cu slab-based scheme as model, because the size of Cu is large in our work (Supplementary Fig. S14). Because the C-C coupling step is key to the C2+ products,[24,25] we first sought to the preferred coupling path on constructed Cu(111) model. Several possible paths, including *CO+*CO, *CO+*CHO, *COH+COH, *CHO+*CH_2O *CO+CHOH and *COH+HCH_2O were considered, and corresponding energies for RDS on Cu(111) are 2.14 eV, 1.24 eV, 0.16 eV, 0.20 eV, 0.54 eV and 0.16 eV (Supplementary Fig. S15), respectively. In comparison, *CHO dimerization (R1 to R3) is exoenergic, thus it was chosen as the basis for subsequent simulations, which is similar to previous reports.[26,27]

$CO(g) + * \rightarrow *CO$ (R1)

$*CO + H^+ + e^- \rightarrow *CHO$ (R2)

$*CHO + *CHO \rightarrow *CHOCHO + *$ (R3)

$*CHO + H^+ + e^- \rightarrow *CH_2O$ (R4)

Interestingly, the energy barrier for the initial hydrogenation step (*CO to *CHO, R2) drops from 0.89 eV over Cu(111) to 0.60 eV over Cu(111)/C_3N_4 interface (Figure 2a and 2b, Supplementary Fig. S16 and S17), indicating the acceleration of CO hydrogenation in the present of g-C_3N_4. Considering water is the hydrogen source in the alkaline electrolyte and g-C_3N_4 is reported to be oxophilicity,[28] we rationally speculate that water dissociation is accelerated around g-C_3N_4 and thus supplies sufficient available hydrogen to undergo CO hydrogenation step. However, not only the *CHO formation but also the following hydrogenation steps (R4) benefit from the existence of g-C_3N_4 around the interface. Consequently, the typical C1 product - methane becomes advantageous around the Cu(111)/C_3N_4 interface compared to C2 product in free energy diagram (FED). For the key branching step, the energy barrier for the transient state (TS) in *CHO hydrogenation step (R4) is only 0.10 eV, which is lower than that in the competitive coupling step (R3, 0.27 eV) around Cu(111)/C_3N_4 interface (Figure 2c, Supplementary Fig. S18). On the contrary, bulk Cu(111) performs higher energy barrier for TS in R4 (0.30 eV) than that in R3 (0.27 eV), resulting in that C2 products is preferable than methane on Cu(111). It seems that *CHO formation and methane formation are simultaneously boosted around Cu(111)/C_3N_4 interface, hence we can deduce that the outstanding performance for acetate over Cu-CN catalysts is not only depending on the Cu(111)/C_3N_4 interface.

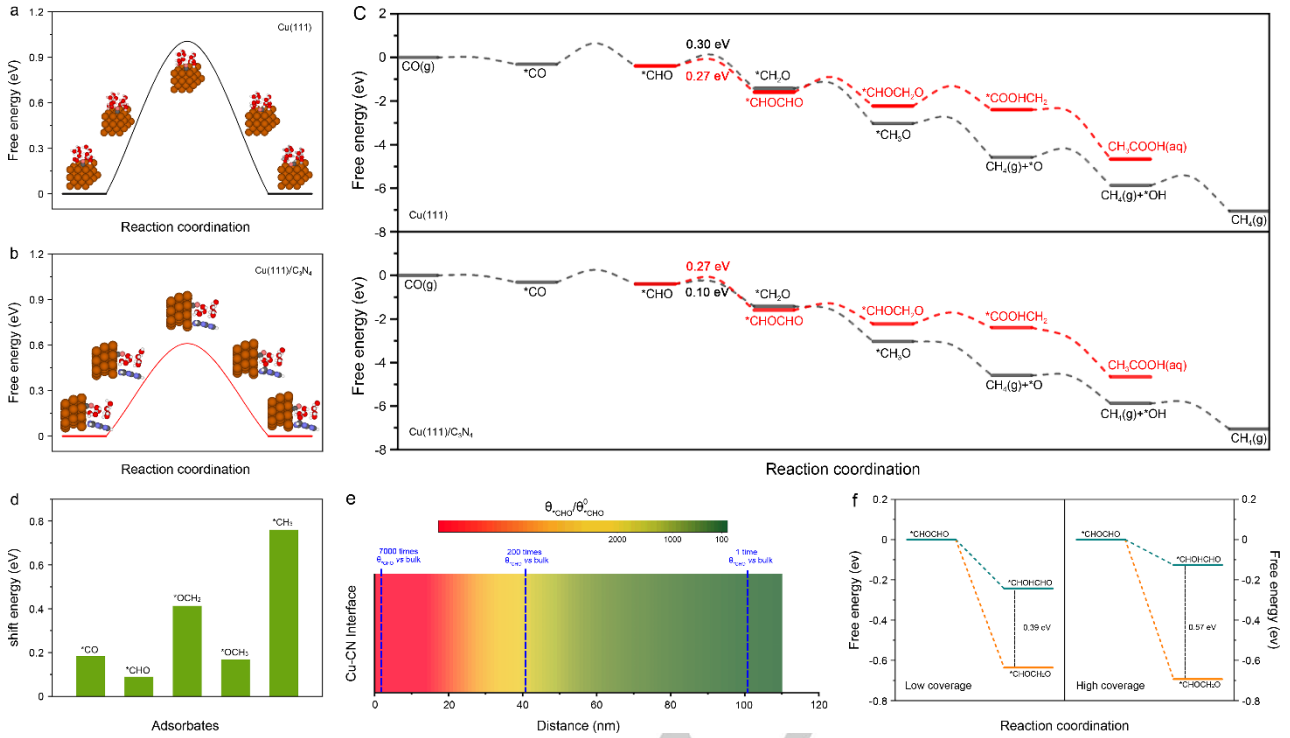

Figure 2. DFT calculations. a, b, The free energy diagram of the hydrogenation of CO into *CHO over Cu(111) and Cu(111)/C_3N_4 models at -0.87 V (vs RHE). c, The free energy diagram of methane and acetic acid path over Cu(111) and Cu(111)/C_3N_4 models at -0.87 V (vs RHE). d, The shift energy of various possible intermediates over Cu(111) surface. e, The plot of ratio of *CHO coverage (in the existence g-C_3N_4) to standard *CHO coverage ($\theta_{CHO}/\theta^0_{CHO}$) versus the distance from Cu(111)/C_3N_4 interface at -0.87 V (vs RHE). f, The free energy diagram of the acetic acid and ethylene/ethanol step in the low (left) and high (right) *CHO coverage on Cu(111) at -0.87 V (vs RHE).

Previous research showed that reaction intermediates can migrate to the appropriate region to undergo the subsequent reaction.[29-32] In light of this view, the migration energy of the possible intermediates was studied (Supplementary Fig. S19). It is noted that the migration energy of *CHO is only 0.09 eV (Figure 2d), suggesting the feasibility for the diffusion of *CHO along Cu(111) surface. Considering that the interfacial effect would be attenuated when *CHO is far from the Cu(111)/C_3N_4 interface, the coupling step is possible to predominate on the Cu(111) surface of supported Cu(111)/C_3N_4 model, which has similar property as bulk Cu(111). However, it is not sufficient to clarify the high selectivity for acetate on the supported catalysts, because the enhanced C-C coupling step also benefits other C2 products. Actually, the migration of *CHO not only makes the coupling route more favorable, but upgrades the overall coverage of *CHO (θ_{CHO}) on the Cu(111) surface. Relative to the *CHO coverage on bulk Cu(111) model (θ^0_{CHO}), the whole level of *CHO coverage (θ_{CHO}) is dramatically promoted by orders of magnitude over Cu(111)/C_3N_4 model. To be specific, the ratio of θ_{CHO} to θ^0_{CHO} shows the negative correlation with the distance to the interface and *CHO coverage (θ_{CHO}) is above 200-fold increase around 40 nm from the interface (Figure 2e), which is favorable to the pathways to acetic acid (R5) and ethylene/ethanol (R6).

$$*CHOCHO + H^+ + e^- \rightarrow *CHOCH_2O \quad (R5)$$

$$*CHOCHO + H^+ + e^- \rightarrow *CHOHCHO \quad (R6)$$

The free energy of R5 decreases from -0.65 eV to -0.71 eV as the *CHO coverage increased, while that of R6 positively moves from -0.26 eV to -0.14 eV, leading the free energy gap between R5 and R6 increases from 0.39 eV to 0.57 eV (Figure 2f). The increased free energy gap suggests that acetic acid path is facilitated and ethylene/ethanol path is relatively restrained by the ascending *CHO coverage, resulting in that the acetic acid dominates over supported Cu(111)/C_3N_4 model in CORR. In this issue, the formation of *CHO is primarily strengthened by the interfacial effect, while the followed *CHO migration enables C-C coupling step and elevates the overall *CHO coverage on the Cu(111) surface, and thus the acetic acid route becomes favorable.

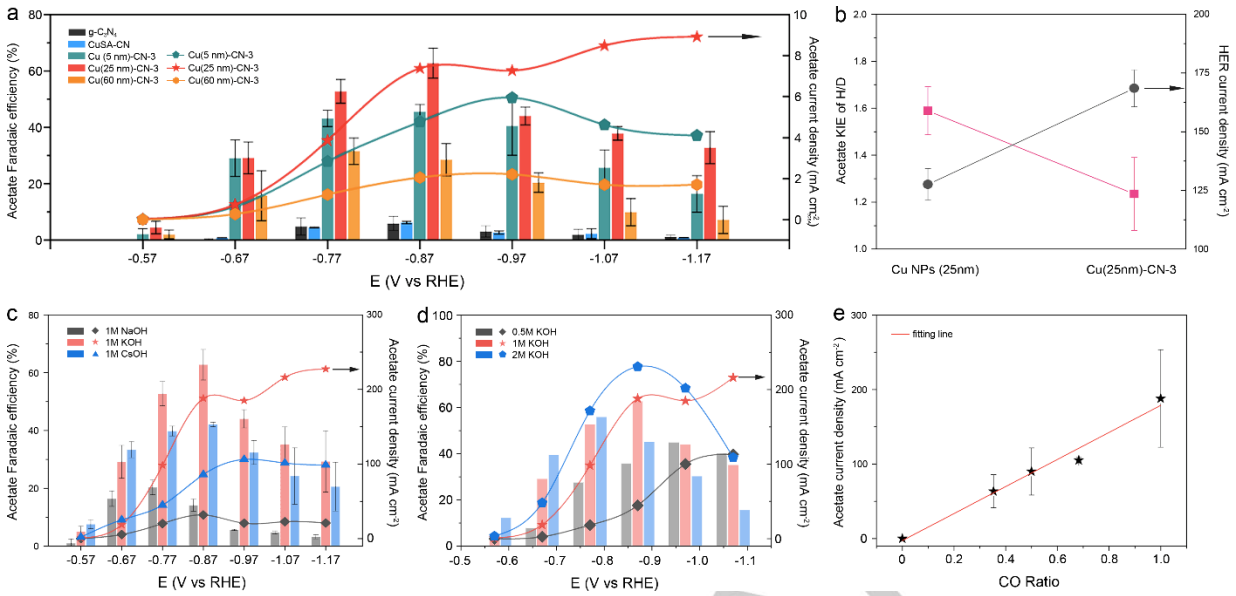

Figure 3. Electrochemical study on Cu-CN catalysts. a, Acetate FEs over Cu-CN catalysts with various size of Cu center and ECSA normalized acetate partial current density over Cu-CN catalysts with various size of Cu center (5 nm, 25 nm and 60 nm) at various applied potentials during CORR. b, The KIE of H/D in CORR to acetate and hydrogen evolution under nitrogen stream at -0.87 V versus RHE on Cu NPs (25nm) and Cu(25nm)-CN-3. c, d, FEs of acetate and corresponding partial current densities on Cu(25nm)-CN-3 in KOH with various concentration (c) and MOH (M=Na^+, K^+ and Cs^+) electrolyte (d) at various applied potentials in CORR. e, Acetate partial current density at -0.87 V versus RHE on Cu(25nm)-CN-3 under the mixed CO/Ar stream with various CO ratio.

DFT simulation results reveal the synergy of dual regions on supported Cu-CN catalyst, and such synergetic effect should be related with the ratio of the Cu/g-C_3N_4 interface and bulk Cu surface (I/S). Hence, we further verified the effect of the ratio of I/S on CORR performance of supported catalysts by controlling the size of Cu NPs in Cu-CN catalysts, because the value of I/S has negative relationship with size of Cu NPs. For comparison, Cu NPs with ~5 nm and ~60 nm were prepared and immobilized on the surface of g-C_3N_4 (Supplementary Fig. S20), and the mass ratio of g-C_3N_4 to Cu NPs was fixed at 3. The g-C_3N_4 loaded Cu single atoms catalyst (CuSA-CN) was also prepared (Supplementary Fig. S21, S22 and Table S7). A volcano-shape trend between the size of Cu NPs and corresponding $FE_{acetate}$ could be observed in CORR (Figure 3a). CuSA-CN showed very low $FE_{acetate}$ (< 10%), indicating that the Cu single sites failed to catalyze the multistep conversion of CO into acetate. In contrast, the supported Cu-CN catalysts with Cu NPs all exhibited the improved catalytic capacity towards acetate production in CORR, and peak acetate FEs were 48.3%, 62.8% and 31.2% over Cu(5nm)-CN-3, Cu(25nm)-CN-3 and Cu(60nm)-CN-3, respectively. Moreover, the ECSA normalized acetate j_{ecsa} over Cu(5nm)-CN-3, Cu(25nm)-CN-3 and Cu(60nm)-CN-3 showed the same trend as the acetate selectivity (Figure 3a, Supplementary Fig. S23, S24 and Table S8), suggesting that the intrinsic activity depended on the particles size. In light of the relationship between particles size and surface area, it is easy to imagine that interface is dominant in Cu(5nm)-CN-3 and bulk Cu surface is dominant in Cu(60nm)-CN-3, which hampers the cooperation of dual region for acetate production. This assumption can also be verified by the FE of methane. Compared with the Cu(25nm)-CN-3, Cu(5nm)-CN-3 generated higher $FE_{methane}$ at most applied potentials (Supplementary Fig. S25) and methane production might be benefited from increased proportion of Cu/C_3N_4 interface over the Cu(5nm)-CN-3, which is consistent with the conclusion obtained in DFT study.

To verify the role of properties of different Cu NPs in the performance disparity towards acetate and methane over Cu-CN catalysts, the CORR performance over Cu-CN and corresponding bulk Cu NPs were compared. Compared to bulk Cu NPs, more methane and acetate were produced over Cu-CN catalysts, indicating that CO molecules tend to be transformed into methane and acetate over Cu in the presence of g-C_3N_4 (Supplementary Fig. S26). It is noting that the production of acetate was significantly enhanced over Cu(25nm)-CN-3 compared with Cu NPs (25nm), while the production of methane showed a slight increase. However, for the Cu(5nm)-CN-3, the production of methane and acetate showed similar increment compared with the Cu NPs (5nm), meaning that the ratio of I/S plays the pivotal role in product selectivity. Moreover, decreased production for other C_{2+} products (ethylene, ethanol and *n*-propanol) over Cu(25nm)-CN-3 and Cu(5nm)-CN-3 confirms the relative suppression of other C_{2+} in the presence of g-C_3N_4, consistent with DFT simulation result. Above results reveal that g-C_3N_4 is key to boost CO conversion and the proper ratio of the interface and Cu surface is significant for acetate production.

DFT simulation results reveal that g-C_3N_4 benefits the hydrogenation steps, we further verify the role of g-C_3N_4 in water dissociation. The kinetic isotopic effect (KIE) of H/D over Cu NPs and Cu-CN catalysts was measured to explore the influence of water activation in acetate formation. The KIEs of H/D is defined by the ratio of the formation rates of acetate in H_2O and D_2O (quantified by the high-performance liquid chromatography), and the KIEs of H/D were 1.59 and 1.23 over Cu NPs (25nm) and Cu(25nm)-CN-3 (Figure 3b), respectively. And at the same applied potential, the current density of H_2 over Cu(25nm)-CN-3 was 168.5 mA cm^{-2}, nearly 1.3-fold to that over Cu NPs (25nm), indicating the enhanced capacity of the water activation over

Cu(25nm)-CN-3. As a result, we can conclude that water activation was enhanced in the presence of g-C_3N_4 and favored the hydrogenation step.

Alkali metal cation is reported to be existed in the form of $M^+(H_2O)_n$, in which the smaller coordination number (*n*) and the radii of cation promote the interaction with the catalysts surface and thus the capability of Cu catalysts to active water.[33-36] Hence, we investigated the performance over Cu(25nm)-CN-3 in various 1M MOH electrolyte (M=Na, K and Cs) in the CORR. While the electrolyte changed from NaOH to KOH (*n*=13 for Na^+, *n*=7 for K^+), the acetate current density was significantly improved from 38 mA cm^{-2} to 188 mA cm^{-2} (Figure 3c), and then dropped slightly to 150 mA cm^{-2} in CsOH (*n*=6 for Cs^+) due to the enhanced competitive HER (hydrogen evolution reaction). The result suggests that the activation of water is closely related with the formation of acetate.

According to previous report,[37] the mass transport can also influence the selectivity of acetate in CORR, and the acetate selectivity will increase with OH^- concentration according to the mass transport mechanism. Thus, the CORR performance over Cu(25nm)-CN-3 in KOH with various concentrations was measured. We can observe the current density of acetate was enhanced from 0.5M to 2M KOH and the potential of peak $FE_{acetate}$ positively shifted (Figure 3d), due to increased conductivity. However, the peak $FE_{acetate}$ in 2M KOH was lower than that in the 1M KOH, indicating that the selectivity of acetate is not proportional to the alkalinity of electrolyte over Cu(25nm)-CN-3. This result was not consistent with the previous reports,[37] suggesting the local mass transport effects were not the main role on the high selectivity of acetate over Cu-CN catalysts.

We further investigate the effect of CO partial pressure on the acetate generation over Cu(25nm)-CN-3 in CORR by using CO/argon mixed gas as the gas source for the linear correlation between partial pressure and coverage on catalyst surface. Obviously, the acetate partial current density linearly increased with the growth of ratio of CO in the mixed gas (Figure 3e) at -0.87 V, indicating the strong positive correlation between the CO partial pressure and acetate activity. The result demonstrates that CO partial pressure is the restrictive factor for acetate formation and C-C coupling is unlikely to be the rate-determining step (RDS) based on previous reports,[13,38] which is consistent with DFT simulation result.

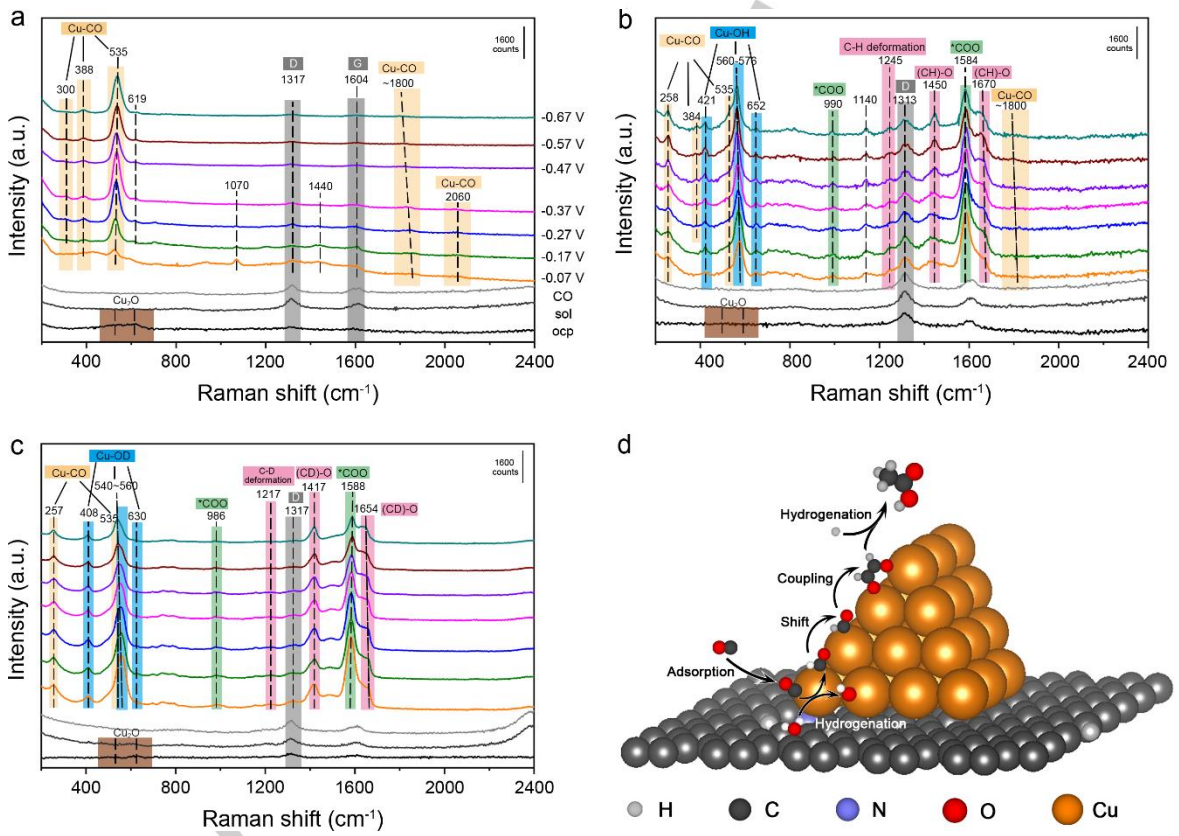

Figure 4. *In-situ* Raman study. a,b, The *in-situ* Raman spectra over Cu NPs (25nm) (a) and Cu(25nm)-CN-3 (b) catalysts at various applied potentials in 1M KOH/H_2O electrolyte. c, The *in-situ* Raman spectra over Cu(25nm)-CN-3 catalyst at various applied potentials in 1M KOH/D_2O electrolyte. d, The illustration of possible reaction mechanism over Cu(25nm)-CN-3.

The *in-situ* surface enhanced Raman spectroscopy (SERS) was then conducted to detect the intermediates in CORR (supplementary Fig. S27). Two characteristic bands around 510 and 625 cm^{-1} (Figure 4a and 4b), belonging to Cu_2O,[39,40] exist before the reaction and disappeared as the potential applied over both Cu NPs (25nm) and Cu(25nm)-CN-3, indicating the reduction of surface cuprous oxide (consistent with XRD results, Supplementary Fig. S28). Other two bands around 1315 and

1600 cm^{-1} are ascribed to the characteristic bands (D and G peak) of carbon paper. On scanning the applied potential from -0.07 V to -0.57 V over Cu NPs (25nm), bands centered around 300, 388 and 535 cm^{-1} (Figure 4a), corresponding to the CO frustrated rotation, Cu-C stretching and Cu-CO,[41,42] appear and exist until the potential removed (supplementary Fig. S29), indicating the adsorption of CO on Cu NPs. Another band related with bridged-bonded CO undergoes the red-shift from 1860 to 1800 cm^{-1} as the potential became negative for the Stack effect,[43,44] while band centered at 2060 cm^{-1}, corresponding to C≡O stretching of linear adsorbed CO on Cu,[44-46] gets distinguishable over Cu NPs (25nm) from -0.47 V, which is viewed as the active adsorbate for subsequent reactions. The results suggested that CO molecules are liable to adsorb on the surface of Cu NPs and linear adsorbed CO are preferentially consumed during CORR. Except band around 2060 cm^{-1}, above CO-related bands emerge over Cu(25nm)-CN-3 but with slight deviation during CORR (Figure 4b), which is likely to be induced by the existence of g-C_3N_4. In addition, certain new bands emerged over the Cu(25nm)-CN-3 compared with the Cu NPs and the g-C_3N_4 (Supplementary Fig. S30). In the low-Raman shift region, bands located at 421, 576 and 652 cm^{-1} appeared since -0.07 V during CORR, which is corresponded to Cu-O_{ad} or Cu-OH species.[47,48] New appeared bands over Cu(25nm)-CN-3 were identified by replacing H_2O with D_2O (Figure 4c) and those bands redshift about 20 cm^{-1} in D_2O, indicating that they are belonging to Cu-OH(D) mode. Furthermore, several new bands appeared over Cu(25nm)-CN-3 in the range of 900 to 1700 cm^{-1}, which are often related with vibration of C-O and C-H species,[42,47,48] and are key to understand the disparity of performance over Cu NPs and Cu-CN catalysts in CORR. Bands around 990 and 1584 cm^{-1} barely shifted in D_2O, which might be ascribed to O-C-O symmetrical stretching and anti-symmetrical stretching of carboxylate species.[49,50] By contrast, bands around 1245, 1450 and 1670 cm^{-1} obviously shifted to 1217, 1417 and 1654 cm^{-1} in D_2O (Figure 4b and 4c, supplementary Fig. S31), suggesting their relation with hydrogen. According the previous reports,[64,65,73] bands centered at 1450 and 1660 cm^{-1} might be assigned to the (CH)-O stretch and asymmetric stretch vibration in intermediates containing *CHO species, and band around 1245 cm^{-1} is attributed to C-H deformation. Moreover, the intensity of bands around 1450 and 1670 cm^{-1} over Cu(25nm)-CN-3 grow as the applied potential negatively shifted, indicating the continuous generation and accumulation of *CHO intermediates. On the contrary, only the Cu-OH species were detected over the Cu(25nm)-CN-3 under N_2 stream (Supplementary Fig. S32). Based on the behaviors of hydrocarbon and carboxylate species characteristic bands, we can assume that hydrocarbon/carboxylate intermediates are easily formed and stabilized on the surface of Cu(25nm)-CN-3. Furthermore, considering the disappearance of linear adsorbed CO and existence of newly emerged Cu-OH species as well as *CHO intermediates over Cu(25nm)-CN-3 compared to Cu NPs (25nm), we conclude that the adsorbed CO is readily hydrogenated over Cu-CN catalysts, in agreement with the DFT simulation results, which is key to the acetate formation in CORR.

Based on above research, we suggest a dual catalytic region mechanism. The CO is primarily reduced into *CHO near the Cu/C_3N_4 interface, and then *CHO intermediates migrate to the Cu surface to undergo the C-C coupling and hydrogenation steps (Figure 4d). The addition of g-C_3N_4 can promote H_2O dissociation and accelerate the reaction *CO+*H_2O→*CHO+*OH. The generated *CHO can transfer to the bulk Cu surface, and the selectivity of acetate can be enhanced by the increased coverage of *CHO.

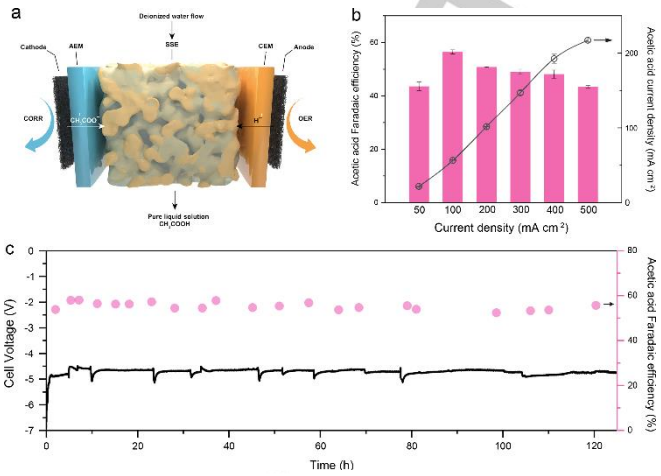

Figure 5. CORR performance over Cu(25nm)-CN-3 in PSE device. a, The illustration of CORR device with porous solid electrolyte. b, The FEs of acetic acid under different current density with pure water as the moving phase. c, long-term operation of the reduction device for acetic acid solution production at constant current density of 100 mA cm^{-2} with water as carrier.

We further sought to apply Cu(25nm)-CN-3 catalyst into a 1-cm^2 electrode device with a proton-conducting porous solid electrolyte (Fig. 5a). In this device, while the water is used as the moving phase in the middle channel, the cathode generated acetate (CH_3COO^-) and anode generated proton (H^+) would be driven by electric field to meet in the middle solid-electrolyte channel to yield acetic acid (CH_3COOH), and the pure product can be obtained without mixing with the electrolyte. Therefore, the using of solid electrolyte and water holds the hope of obtaining pure acetic acid solution without further separation and purification. Under a releasing deionized water flow rate of 50 mL h^{-1}, acetic acid was produced as the major product under various current density (50, 100, 200, 300, 400 and 500 mA cm^{-2}) in the device, and peak acetic acid FE of 56.5 % was achieved at constant current density of 100 mA cm^{-2} (Fig. 5b, Supplementary Fig. S33 and Table S9). More important, acetic acid could be continuously yielded over Cu(25nm)-CN-3 in our device for 120 h around -4.45 V with negligible performance decay (FE>55%, j_{total}≈100 mA cm^{-2}), resulting in a total of 90 mM CH_3COOH product (Figure 4c). ^1H NMR analyses revealed the high purity (>90%) (Supplementary Fig. 34). In addition, we can observe that the change of the Cu(25nm)-CN-3 was not notable after the reaction, suggesting that the catalyst was stable (Supplementary, Fig. S35). The result suggests that the Cu(25nm)-CN-3 holds the promising potential to achieve the efficient commercial production of acetic acid directly from CO and electricity.

Conclusion

Cu NPs of suitable size supported on g-C_3N_4 are highly efficient in CORR to acetate. The FE of 62.8% and partial current density

of 188 mA cm^{-2} can be achieved over Cu(25nm)-CN-3. The cooperation of the two catalytic regions is responsible for the superior performance. The hydrogenation of CO is boosted around the Cu/C_3N_4 interface and the formed *CHO intermediates migrate to the bulk surface of Cu from the interface to undergo the following coupling and hydrogenation step to form acetate. The coverage of *CHO on the Cu NPs in Cu(25nm)-CN-3 is much larger than that on Cu NPs without the support, which promotes the formation of acetate. Furthermore, high purity acetic acid(>90%) solution is produced by using the solid-electrolyte CO reduction device at the constant current density of 100 mA cm^{-2} for at least 120 h, indicating the great potential of Cu(25nm)-CN-3 for the efficient commercial production of acetic acid from CO and electricity.

Acknowledgements

The authors thank the National Natural Science Foundation of China (22003070, 22033009, 22293015, 21890761, 22293015, 22121002), National Key Research and Development Program of China (2020YFA0710203), and Photon Science Center for Carbon Neutrality. The operando X-ray adsorption spectroscopy (XAS) measurements were performed using a flow cell at the 1W1B, 1W2B beamline at Beijing Synchrotron Radiation Facility.

Keywords: Green Chemistry • Carbon monoxide • Electrocatalysis • Acetic acid • Porous solid electrolyte

[1] P. Kalck, C. Le Berre, P. Serp, *Coord. Chem. Rev.* **2020**, *402*, 213078.
[2] Q. Qian, J. Zhang, M. Cui, B. Han, *Nat. Commun.* **2016**, *7*, 11481.
[3] N. v. Kutepow, W. D. Himmele, H. Hohenschutz, *Chem Ing Tech (Weinh)* **1965**, *37*, 383-388.
[4] F. Fischer, *Ind. Eng. Chem.* **1925**, *17*, 574-576.
[5] Y. Lum, T. Cheng, W. A. Goddard, 3rd, J. W. Ager, *J. Am. Chem. Soc.* **2018**, *140*, 9337-9340.
[6] M. Jouny, G. S. Hutchings, F. Jiao, *Nat. Catal.* **2019**, *2*, 1062-1070.
[7] M. Jouny, W. Luc, F. Jiao, *Nat. Catal.* **2018**, *1*, 748-755.
[8] F. Calle-Vallejo, M. T. Koper, *Angew. Chem. Int. Ed.* **2013**, *52*, 7282-7285.
[9] D. Raciti, L. Cao, K. J. T. Livi, P. F. Rottmann, X. Tang, C. Li, Z. Hicks, K. H. Bowen, K. J. Hemker, T. Mueller, C. Wang, *ACS Catal.* **2017**, *7*, 4467-4472.
[10] Y. Ji, Z. Chen, R. Wei, C. Yang, Y. Wang, J. Xu, H. Zhang, A. Guan, J. Chen, T.-K. Sham, J. Luo, Y. Yang, X. Xu, G. Zheng, *Nat. Catal.* **2022**, *5*, 251-258.
[11] D. Gao, P. Wer, H. Li, L. Lin, G. Wang, X. Bao, *Acta Phys. -Chim. Sin.* **2021**, *37*, 2009021.
[12] C. Xia, P. Zhu, Q. Jiang, Y. Pan, W. Liang, E. Stavitski, H. N. Alshareef, H. Wang, *Nat. Energy* **2019**, *4*, 776-785.
[13] P. Zhu, C. Xia, C. Y. Liu, K. Jiang, G. Gao, X. Zhang, Y. Xia, Y. Lei, H. N. Alshareef, T. P. Senftle, H. Wang, *Proc. Natl. Acad. Sci. USA* **2021**, *118*, e2111521118.
[14] X. Chang, A. Malkani, X. Yang, B. Xu, *J. Am. Chem. Soc.* **2020**, *142*, 2975-2983.
[15] S. H. Lee, J. C. Lin, M. Farmand, A. T. Landers, J. T. Feaster, J. E. Aviles Acosta, J. W. Beeman, Y. Ye, J. Yano, A. Mehta, R. C. Davis, T. F. Jaramillo, C. Hahn, W. S. Drisdell, *J. Am. Chem. Soc.* **2021**, *143*, 588-592.
[16] P. Munnik, P. E. de Jongh, K. P. de Jong, *Chem. Rev.* **2015**, *115*, 6687-6718.
[17] W. Gao, Z. D. Hood, M. Chi, *Acc. Chem. Res.* **2017**, *50*, 787-795.
[18] L. Zuburtikudis, H. Saltsburg, *Science* **1992**, *258*, 1337-1339.
[19] C. Choi, T. Cheng, M. Flores Espinosa, H. Fei, X. Duan, W. A. Goddard, 3rd, Y. Huang, *Adv. Mater.* **2019**, *31*, e1805405.
[20] Z. Han, Y. Yu, W. Zheng, Y. Cao, *New J. Chem.* **2017**, *41*, 9724-9730.
[21] C. Chen, X. Yan, S. Liu, Y. Wu, Q. Wan, X. Sun, Q. Zhu, H. Liu, J. Ma, L. Zheng, H. Wu, B. Han, *Angew. Chem. Int. Ed.* **2020**, *59*, 16459-16464.
[22] O. A. Baturina, Q. Lu, M. A. Padilla, L. Xin, W. Li, A. Serov, K. Artyushkova, P. Atanassov, F. Xu, A. Epshteyn, T. Brintlinger, M. Schuette, G. E. Collins, *ACS Catal.* **2014**, *4*, 3682-3695.
[23] C. Choi, S. Kwon, T. Cheng, M. Xu, P. Tieu, C. Lee, J. Cai, H. M. Lee, X. Pan, X. Duan, W. A. Goddard, Y. Huang, *Nat. Catal.* **2020**, *3*, 804-812.
[24] T. Li, C. Yang, J.-L. Luo, G. Zheng, *ACS Catal.* **2019**, *9*, 10440-10447.
[25] Z. Z. Niu, F. Y. Gao, X. L. Zhang, P. P. Yang, R. Liu, L. P. Chi, Z. Z. Wu, S. Qin, X. Yu, M. R. Gao, *J. Am. Chem. Soc.* **2021**, *143*, 8011-8021.
[26] W. Ma, S. Xie, T. Liu, Q. Fan, J. Ye, F. Sun, Z. Jiang, Q. Zhang, J. Cheng, Y. Wang, *Nat. Catal.* **2020**, *3*, 478-487.
[27] X. Yan, C. Chen, Y. Wu, S. Liu, Y. Chen, R. Feng, J. Zhang, B. Han, *Chem. Sci.* **2021**, *12*, 6638-6645.
[28] Y. Chen, Q. Zhou, G. Zhao, Z. Yu, X. Wang, S. X. Dou, W. Sun, *Adv. Funct. Mater.* **2018**, *28*, 1705583.
[29] H. Yin, Y. Shen, W. Xi, X. Liu, S. Yin, J. Jia, J. Zhang, Y. Ding, *Small Methods* **2022**, *6*, 2101328.
[30] B. Hu, Y. Yin, G. Liu, S. Chen, X. Hong, S. C. E. Tsang, *J. Catal.* **2018**, *359*, 17-26.
[31] H. Yang, F. R. Negreiros, Q. Sun, M. Xie, L. Sementa, M. Stener, Y. Ye, A. Fortunelli, W. A. Goddard, III, T. Cheng, *ACS Appl. Mater. Interfaces* **2021**, *13*, 31554-31560.
[32] M. Zhu, P. Tian, M. E. Ford, J. Chen, J. Xu, Y.-F. Han, I. E. Wachs, *Acs Catal.* **2020**, *10*, 7857-7863.
[33] M. Mikkelsen, M. Jørgensen, F. C. Krebs, *Energy Environ. Sci.* **2010**, *3*, 43-81.
[34] D. U. Nielsen, X.-M. Hu, K. Daasbjerg, T. Skrydstrup, *Nat. Catal.* **2018**, *1*, 244-254.
[35] M. Aresta, A. Dibenedetto, A. Angelini, *Chem.Rev.* **2014**, *114*, 1709-1742.
[36] W. Ma, S. Xie, X.-G. Zhang, F. Sun, J. Kang, Z. Jiang, Q. Zhang, D.-Y. Wu, Y. Wang, *Nat. Commun.* **2019**, *10*, 892.
[37] H. H. Heenen, H. Shin, G. Kastlunger, S. Overa, J. A. Gauthier, F. Jiao, K. Chan, *Energy Environ. Sci.* **2022**, *15*, 3978-3990.
[38] X. Chang, J. Li, H. Xiong, H. Zhang, Y. Xu, H. Xiao, Q. Lu, B. Xu, *Angew. Chem. Int. Ed.* **2022**, *61*, e202111167.
[39] R. M. Hammaker, S. A. Francis, R. P. Eischens, *Spectrochim. Acta* **1965**, *21*, 1295-1309.
[40] Y. Kwon, Y. Lum, E. L. Clark, J. W. Ager, A. T. Bell, *ChemElectroChem* **2016**, *3*, 1012-1019.
[41] I. V. Chernyshova, P. Somasundaran, S. Ponnurangam, *Proc. Natl. Acad. Sci. USA* **2018**, *115*, E9261-E9270.
[42] S. Jiang, K. Klingan, C. Pasquini, H. Dau, *J. Chem. Phys.* **2019**, *150*, 041718.
[43] Y. Zhao, X. Chang, A. S. Malkani, X. Yang, L. Thompson, F. Jiao, B. Xu, *J. Am. Chem. Soc.* **2020**, *142*, 9735-9743.
[44] S. Zou, M. J. Weaver, *J. Phys. Chem.* **1996**, *100*, 4237-4242.
[45] B. D. Smith, D. E. Irish, P. Kedzierzawski, J. Augustynski, *J. Electrochem. Soc.* **1997**, *144*, 4288.
[46] K. G. Schmitt, A. A. Gewirth, *J. Phys. Chem. C* **2014**, *118*, 17567-17576.
[47] M. Moradzaman, G. Mul, *ChemElectroChem* **2021**, *8*, 1478-1485.
[48] H. An, L. Wu, L. D. B. Mandemaker, S. Yang, J. de Ruiter, J. H. J. Wijten, J. C. L. Janssens, T. Hartman, W. van der Stam, B. M. Weckhuysen, *Angew. Chem. Int. Ed.* **2021**, *60*, 16576-16584.
[49] Y. Ichinohe, T. Wadayama, A. Hatta, *J Raman Spectrosc* **1995**, *26*, 335-340.
[50] W. Shan, R. Liu, H. Zhao, Z. He, Y. Lai, S. Li, G. He, J. Liu, *ACS Nano* **2020**, *14*, 11363-11372.

10.1002/anie.202301507

Entry for the Table of Contents

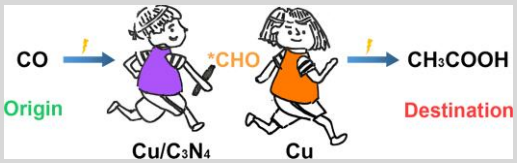

The electrocatalyst composed of Cu nanoparticles and *g*-C_3N_4 nanosheets (Cu-CN) is reported, which could efficiently catalyze CO into acetate with a Faradaic efficiency of 62.8% in a flow cell and acetic acid continuously in a porous solid electrolyte reactor. *In-situ* experiments and density functional theory studies reveal the synergy between dual catalytic regions: Cu/C_3N_4 interface enhance the generation and coverage of *CHO from CO, and Cu NPs facilitate the acetic acid (acetate) generation from migrated *CHO.